RSC Advances

PAPER

View Article Online
View Journal | View Issue



Cite this: *RSC Adv.*, 2025, **15**, 32536

# Martensite-like phase transformation of ligand-capped SnS tetrahedrons from π phase to α phase and its impact on $H_2$ evolution performance

Xiangxin Du, Kenji Kazumi, Toru Utsunomiya, Isshin Sumiyoshi and Yoshitaro Nose *

π-Tin sulfide (SnS) is an emerging semiconductor of interest with attractive properties for applications in solar energy conversion and non-linear optics. However, its intrinsic metastability raises concerns and requires further investigation. Here, we report a newly discovered martensite-like phase transition in ligand-capped π-SnS tetrahedrons by a post-annealing treatment. By adjusting the annealing temperature, we found that the desorption of surface ligands initiated the rearrangement of surface atoms, thus triggering a chain phase transformation from π phase to α phase through the displacement of adjacent atoms. Large amounts of boundaries and stacking faults were present in this process, as shown from high-resolution transmission electron microscopy combined with selected area electron diffraction. Furthermore, X-ray diffraction, X-ray photoelectron spectroscopy, and Fourier-transform infrared spectroscopy showed that the initiation temperature for phase transition relies on surface ligands. Hexamethyldisilazane (HMDS)-capped tetrahedrons show higher stability against a temperature of 500 °C than oleylamine (OLA)-capped tetrahedrons due to the stronger interaction between HMDS ligands with SnS surface atoms. The mechanism involved in the ligand-affected structure evolution of π-SnS tetrahedrons and the corresponding $H_2$ generation performance is discussed in detail.

Received 25th May 2025
Accepted 30th August 2025

DOI: 10.1039/d5ra03669k

rsc.li/rsc-advances



## 1. Introduction

IV–VI Compound semiconductors have attracted significant attention for their potential applications in various fields including solar cells, optoelectronic devices, and near-infrared (NIR) detectors. Especially, π-phase monochalcogenides such as SnS, GeS, SnSe and GeSe have emerged as promising materials due to their cubic structure and larger optical bandgaps compared to the conventional α phases.[1,2] Among these monochalcogenides, π-SnS has been widely investigated because of its experimental feasibility and low cost. π-SnS exhibits a cubic structure ($P2_13$) with a 64-atom unit cell and the calculated lattice parameter is $a = 11.7$ Å.[3] The reported optical bandgap of π-SnS ranges from 1.5 to 1.8 eV,[1,4,5] indicating a more effective optical absorption, which makes it a promising candidate for efficient solar energy conversion. For instance, a solar cell with an absorber layer of π-SnS has achieved a conversion efficiency of 1.28%.[6] Besides, π-SnS particles have demonstrated favorable photocatalytic activity.[7,8]

Paradoxically, π-SnS is a metastable phase as its formation energy is computed to be 2.19 kJ $mol^{-1}$ higher than that of the orthorhombic ground state (α-SnS).[9] Understanding the thermodynamic stability and solid–solid phase transition is crucial to control phase-dependent properties and applications. Experimentally, π-SnS has been observed to be kinetically stable at room temperature. To date, π-SnS films have been obtained by a variety of techniques including chemical bath deposition,[10] thermal evaporation,[11] atomic layer deposition[12] and spray pyrolysis.[13] Under an inert gas atmosphere, the thin films are thermally stable up to 300–400 °C, while over 400 °C secondary phases like $SnS_2$ and metallic Sn were observed.[14–16] The particles of π-SnS with various shapes, typically tetrahedrons and spheres, are synthesized using colloidal (surfactant-assisted) methods.[17–19] Greyson *et al.* reported that these microcrystals remain stable at 300 °C for 3 h under Ar atmosphere but transform into α-SnS at 250 °C in oleylamine.[20]

The phase stability of particles is often affected by the relative contribution of surface energies to the total Gibbs free energy. High surface energy allows surface atoms to rearrange to achieve the ground state. Such situations can typically be alleviated by impurity incorporation or particle agglomeration, thereby maintaining the stability of metastable phases. Density-functional theory (DFT) calculations demonstrated that the metastable π-SnS particles may be effectively stabilized by surface ligands.[21] Several interesting reports are also available on the meta-stability of ligand-capped π-SnS with annealing temperature. The triethanolamine-capped nanoparticles were stable up to 400 °C and partly transformed to the orthorhombic phase at 450 °C under vacuum for 1 h.[19] Fridman *et al.*[22]

*Department of Materials Science and Engineering, Kyoto University, Sakyo-ku, Kyoto, 606-8501, Japan. E-mail: nose.yoshitaro.5e@kyoto-u.ac.jp*

reported the high phase stability at 400 °C of polyvinylpyrrolidone-capped π-SnS nano-cubes. Little difference in the impact of different surface ligands on the stability of π-SnS nanoparticles was seen. However, the intrinsic properties of surface ligands were proved to be crucial to the $H_2$ evolution performance of π-SnS in our previous work[23] and, logically, to its physicochemical properties. In the present work, we report on an isothermal annealing study for oleylamine (OLA)-capped π-SnS particles and hexamethyldisilazane (HMDS) & OLA-capped π-SnS particles, respectively. The temperature- and time-dependent phase transition behavior and its effect on particles' morphology are investigated. The mechanism involved in the ligand-affected phase stability and transformations, as well as the associated structure evolution, is detailed using X-ray diffraction, X-ray photoelectron spectroscopy, Fourier-transform infrared spectroscopy and high-resolution transmission electron microscopy. Notably, a martensite-like phase transformation in SnS is proposed for the first time.

## 2. Experimental

### 2.1. Materials

Tin(II) chloride ($SnCl_2$, 97%, Wako Pure Chemical Industries, Ltd.) and elemental sulfur powder ($S_8$, 99.99%, Kojundo Chemical Laboratory Co., Ltd.) were used as raw materials without further purification. Oleylamine (OLA, FUJIFILM Wako Pure Chemical Corporation) and hexamethyldisilazane (HMDS, Apolloscientific.co.uk) were used as a solvent and ligands. Sodium sulfite ($Na_2SO_3$, 97%), sodium sulfide nonahydrate ($Na_2S \cdot 9H_2O$, 96%) and hydrogen hexachloroplatinate (IV) hexahydrate ($H_2PtCl_6 \cdot 6H_2O$) were purchased from Nacalai Tesque, Inc. and used for hydrogen evolution experiments. Purified water (18.2 MΩ cm) was obtained from a filtration system (Direct-Q UV3, Merck & Co., Inc.).

### 2.2. Preparation method

**2.2.1. Synthesis of π-SnS particles.** π-SnS particles were synthesized *via* a solvothermal method adopted from our previous work. In a typical procedure, 0.3640 g of $SnCl_2$ and 0.0744 g of elemental sulfur were dissolved in 32 mL of oleylamine (OLA) under magnetic stirring and heating. After 15 min, 0.8 mL of hexamethyldisilazane (HMDS) was introduced into the solution. Upon formation of a transparent and homogeneous precursor, the mixture was transferred to a 50 mL Teflon-lined stainless-steel autoclave and heated at 200 °C for 5 h. Throughout the synthesis, a continuous $N_2$ flow was maintained to prevent oxidation and moisture absorption. The resulting precipitate was washed four times with ethanol and air-dried. The obtained samples were labeled as OSNS (OLA-capped π-SnS) and HSNS (HMDS & OLA-capped π-SnS), respectively.

**2.2.2 Post-annealing treatment.** The as-prepared π-SnS particles were subjected to post-annealing in a quartz boat under an $N_2$ atmosphere at temperatures of 400, 500, 600, and 650 °C (see Fig. S1 for the temperature profile). After annealing, the furnace was turned off, and the powder was allowed to cool naturally to room temperature. The samples after annealing were labeled as OSNS/HSNS-400, OSNS/HSNS-500, OSNS/HSNS-600, and OSNS/HSNS-650, respectively.

### 2.3. Characterization and $H_2$ evolution measurement

Field emission scanning electron microscopy (FE-SEM, JSM-6500, JEOL) was used to characterize the morphology of SnS particles. X-ray diffraction was conducted using the X-ray diffractometer (XRD, Empyrean, Malvern Panalytical) with Cu Kα at 45 kV and 40 mA to identify the phases and crystal structure. The surface chemistry of SnS particles was characterized through X-ray photoelectron spectroscopy (XPS, ESCA-3400, Shimadzu) using Mg Kα (1.253 keV) with an operating voltage of 10 kV and a current of 20 mA. Fourier-transform infrared spectroscopy (FT-IR, INVENIO, BRUKER) was further measured to confirm the existence of surface ligands. The transmittance spectrum was measured by a UV–vis spectrophotometer (UV-2600, Shimadzu) to evaluate the optical properties. High-resolution transmission electron microscopy (HRTEM, JEM-2100F, JEOL) and selected area electron diffraction (SAED) were measured to analyze the precise morphology of particles and the corresponding crystal phase. $H_2$ evolution performance of SnS particles was evaluated by a gas chromatograph (CGC-001T, J-Science Lab) under irradiation from a 300 W xenon lamp.

## 3. Results and discussion

The typical morphologies of SnS particles before and after annealing are shown in Fig. 1. As revealed in Fig. 1(a), OSNS exhibited regular nano- and micro-tetrahedrons with clear edges and several truncated tetrahedrons, which were also reported by Deng *et al.*[24] A high degree of roughness was observed on the surfaces (inset figure). HSNS (Fig. 1(b)) also exhibits a tetrahedral shape but with reduced roughness, suggesting that HMDS may change the surface state of the tetrahedrons. After annealing at 400 °C, the surfaces became smoother (Fig. 1(c) and (d)), with the formation of several concave pits. For OSNS-400, the surface roughness was still observed on the small-sized tetrahedrons. Increasing the temperature to 650 °C, the tetrahedral structure became deformed and fragmented. As shown in Fig. 1(e) and (f), the edges of the tetrahedrons became indistinct, while severe concave pits, cracks and chips developed. In addition, the number of such defective particles gradually increased as the temperature rose, as seen in Fig. S2.

Fig. 2 shows XRD profiles of SnS particles under various annealing conditions. In Fig. 2(a), the peaks detected in OSNS conform well to the cubic π-SnS with a space group of $P2_13$ (PDF #04-023-2702, $a = b = c = 11.60$ Å). After annealing at 400 °C for 10 minutes (OSNS-400), the cubic phase was maintained. While in OSNS-500, several diffractions attributed to the orthorhombic α-SnS (PDF #03-065-3812, *Pnma*, $a = 4.34$ Å, $b = 11.20$ Å, $c = 3.99$ Å) were observed, indicating that some π-SnS particles had transformed into α-SnS at 500 °C. The diffractions are significantly enhanced in OSNS-600 and dominated in OSNS-650, indicating that cubic π-SnS gradually transformed

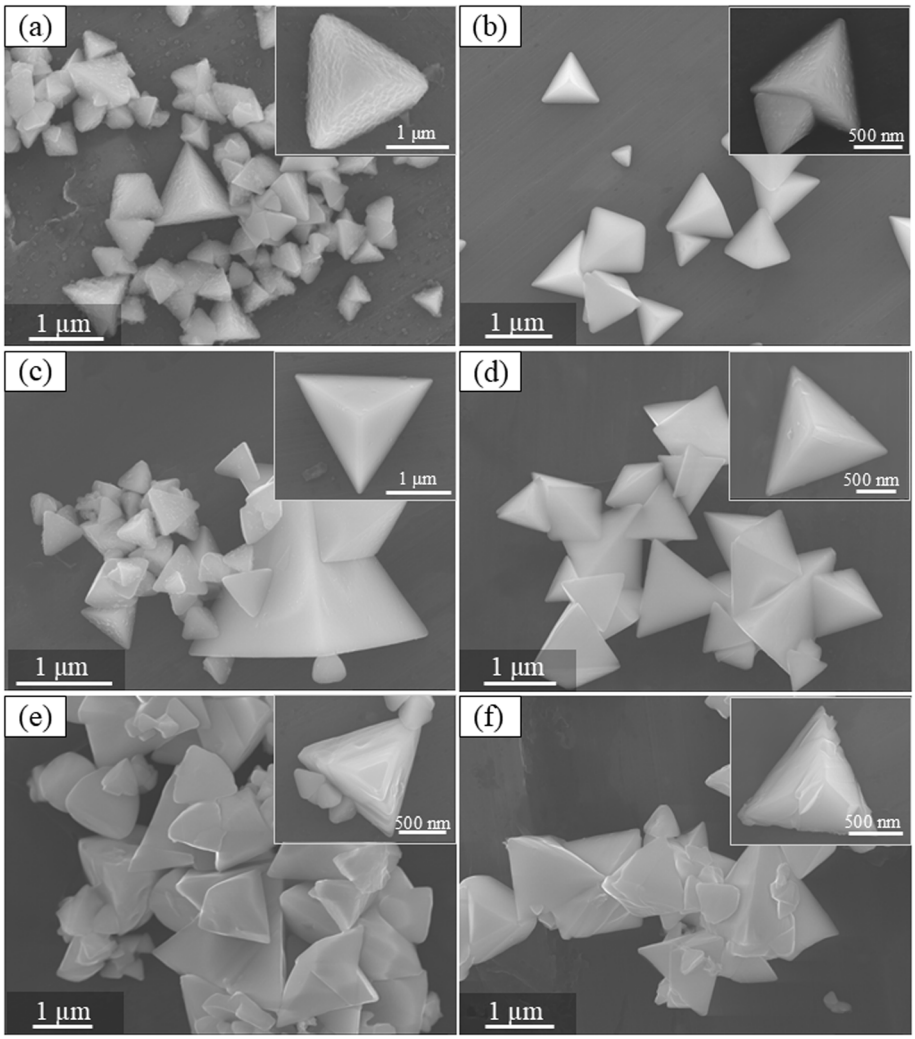


Fig. 1 SEM images of OLA/HMDS-capped SnS particles before and after annealing. (a) OSNS, (b) HSNS, (c) OSNS-400, (d) HSNS-400, (e) OSNS-650 and (f) HSNS-650.

into orthorhombic α-SnS with increased temperatures. Meanwhile, a small diffraction peak was observed around 22–24° (Fig. S3) in OSNS-600 and OSNS-650. This diffraction comes from the elemental tin, which crystallized during the cooling process, owing to the escape of sulfur atoms at high annealing temperatures. Such sulfur loss is a common phenomenon in SnS when annealed in an inert atmosphere due to the high vapor pressure of sulfur.[25–27]

Fig. 2(b) shows the effect of annealing time on OSNS samples. Since no impurity phases are present, the fraction of π-SnS was evaluated using the relative intensity of diffractions expressed by the following equation:

$$R_{400} = \frac{I_{\pi 400}}{I_{\pi 400} + I_{\alpha 040}},$$

where $R_{400}$ represents the intensity ratio of (400) diffraction from π-SnS. $I_{\pi 400}$ and $I_{\alpha 040}$ are the peak intensities of (400) and (040) diffractions of π-SnS and α-SnS, respectively. As shown in Fig. 2(b), $R_{400}$ of OSNS-400 remained 100% from 10 min to 1 h, but decreased to 84.51% after 5 h of annealing, indicating a slight phase transition to α-SnS. In OSNS-500, nearly half of the SnS particles transformed to the α phase, with 54.39% π phase left. However, it exhibited non-linear behavior with the annealing time from 10 min to 5 h. A similar trend was observed in OSNS-600 and OSNS-650. Within 30 min, $R_{400}$ dropped to 0% in OSNS-650, suggesting a rapid and complete phase transition from π phase to α phase. Interestingly, the π phase reappeared with prolonged annealing: the $R_{400}$ values of 3.11% and 23.80% at 1 and 5 h, respectively.

As reported in our previous work, HMDS promotes the formation of highly crystalline π-SnS tetrahedrons. The thermal stability of such tetrahedrons was also evaluated. Fig. 2(c) shows the XRD profiles of HSNS samples before and after annealing for 10 min. Unlike OSNS, weak diffractions from α-SnS were detected at 400 °C and 500 °C in HSNS, which stems from the participation of the ligands: HMDS. Surprisingly, the fraction of π-SnS remains higher with $R_{400}$ staying above 90% as annealing time increases (Fig. 2(d)), indicating that the addition of HMDS may promote the stability of the particles. HSNS-600 and HSNS-

 

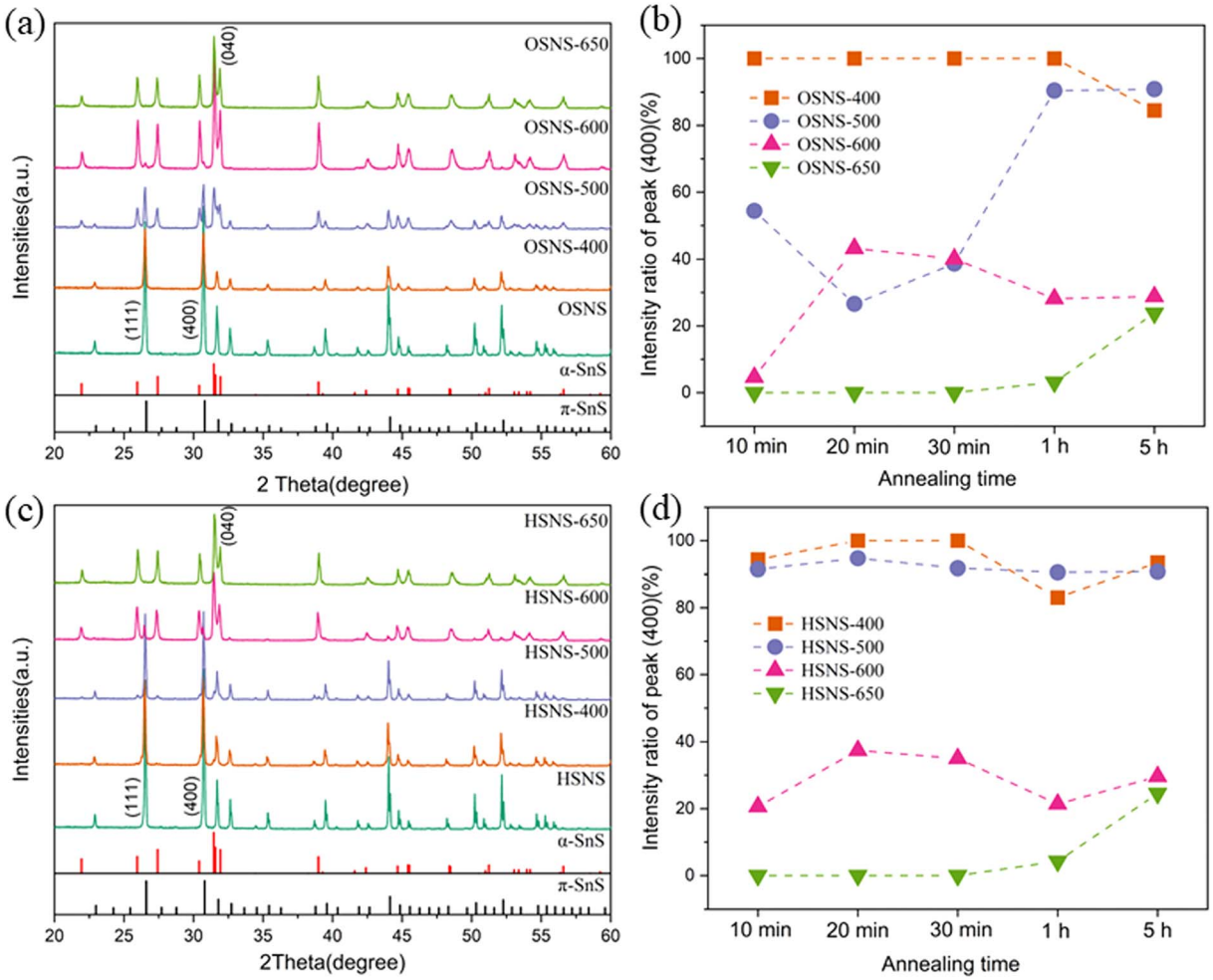


Fig. 2 Crystal structure of OLA/HMDS-capped SnS particles before and after annealing. (a) XRD pattern of OSNS samples annealed for 10 min. (b) Intensity ratio of the (400) peak from XRD analysis over time. (c) XRD pattern of HSNS samples annealed for 10 min. (d) Corresponding intensity ratio of the (400) peak over time.

650 show a similar phase behavior to OSNS samples. Gautam *et al.* reported a "reversible" transformation phenomenon in titanium dioxide between the rutile and anatase phases.[28] Similar behavior was observed in our SnS particles OSNS-650 and HSNS-650. This may originate from a slight difference in the formation energies of α-SnS and π-SnS, but the detailed mechanism will be discussed in further studies. To assess the long-term phase stability, all samples were stored under ambient atmospheric conditions for six months prior to repeated XRD characterization. The diffraction patterns (Fig. S4) reveal excellent phase stability, with nearly identical crystallographic features observed before and after aging. Notably, both the pristine π-phase and completely converted α-phase specimens showed no measurable structural degradation. Intriguingly, samples that had undergone partial phase transformation displayed subtle but detectable fluctuations in π-phase content (Table 1), providing additional evidence for the reversible interconversion between π and α phases.

XPS and FT-IR measurements were conducted to confirm the presence of surface ligands and the related surface behavior of SnS before and after annealing for 10 min. The XPS spectra of Sn 3d (Fig. 3(a)) reveal the coexistence of $Sn^{4+}$ and $Sn^{2+}$ in all samples. The peaks at 488.0 and 496.5 eV in OSNS correspond to $3d_{5/2}$ and $3d_{3/2}$ states of $Sn^{4+}$, respectively, and the peaks at 486.4 and 494.9 eV are attributed to the states of $Sn^{2+}$.[29–31] A similar spectrum is observed in OSNS-400, while the peaks shift to lower energy in samples OSNS-500, OSNS-600 and OSNS-650. The presence of $Sn^{4+}$ is attributed to the oxidation of surface $Sn^{2+}$ during high-temperature annealing or the sample preparation process for XPS. The S 2p spectra in Fig. 3(b) are mainly deconvoluted into two peaks corresponding to S $2p_{3/2}$ and S $2p_{1/2}$ orbitals. As observed in the case of Sn, the S 2p spectrum of OSNS-400 is similar to that of OSNS, while a slight energy

Table 1 The content of the π phase of OSNS/HSNS samples

| Content (%) | — | −400 | −500 | −600 | −650 |
|---|---|---|---|---|---|
| OSNS | 100 | 100 | 54.39 | 4.6 | 0 |
| OSNS (6 months) | 100 | 100 | 55.16 | 7.41 | 0 |
| HSNS | 100 | 94.37 | 91.49 | 20.61 | 0 |
| HSNS (6 months) | 100 | 86.95 | 84.81 | 35.08 | 0 |

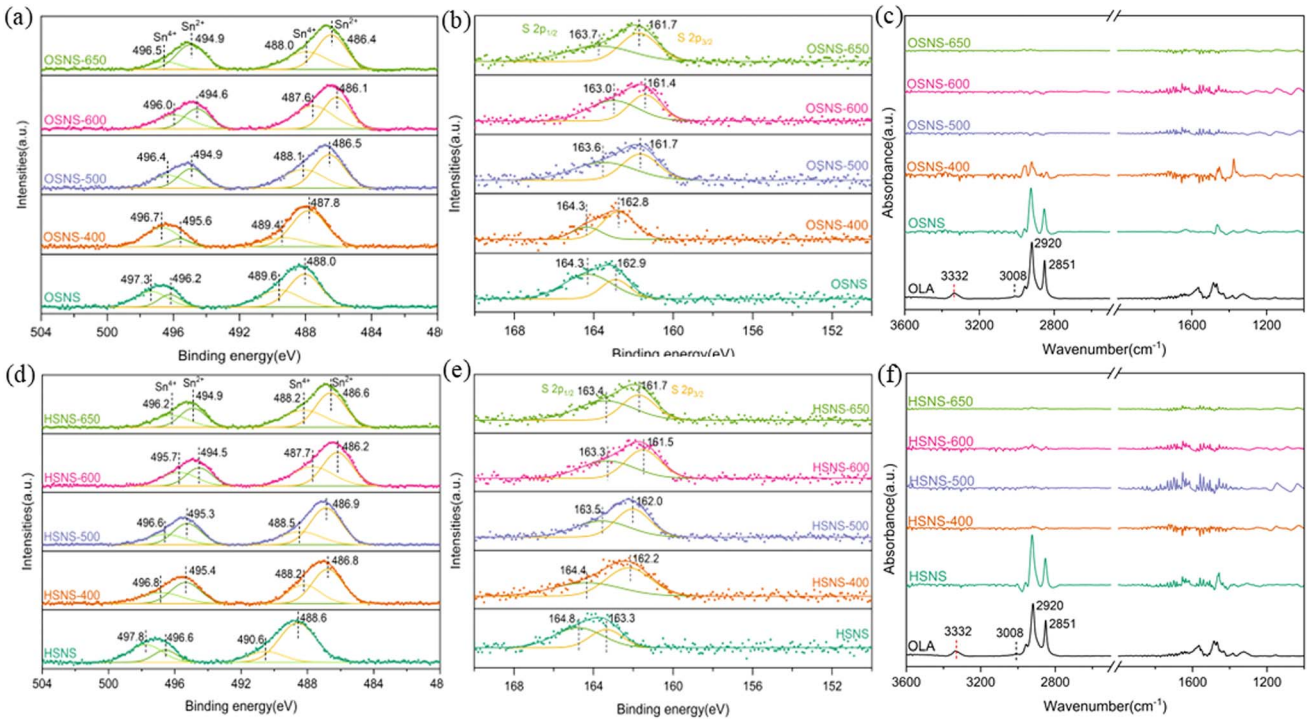


Fig. 3 (a) Sn 3d, (b) S 2p XPS spectra, and (c) FT-IR spectra of OSNS samples. (d) Sn 3d, (e) S 2p XPS spectra, and (f) FT-IR spectra of HSNS samples.

shift is exhibited in the samples annealed at higher temperatures. The energy shift of Sn 3d and S 2p is well consistent with the surface ligand behavior shown in Fig. 3(c). The symmetric and asymmetric stretching vibrations of the methylene group ($-CH_2$) at 2851 and 2920 $cm^{-1}$ from pure OLA were also observed in OSNS, indicating that OLA molecules were successfully capped on the surface of the synthesized SnS particles. The marked peak at 3332 $cm^{-1}$ originates from the symmetric stretching vibration of the amine group ($-NH_2$), which was absent in the spectra of OSNS. This signal is suppressed by the oriented interaction between the amine group and the Sn atoms on the SnS surface.[32] In OSNS-400, the signals from $-CH_2$ were much weakened, meaning that large amounts of OLA ligands desorbed from the surfaces after annealing at 400 °C for 10 min. No signal from OLA was observed at higher temperatures, indicating that the interacting OLA ligands desorbed completely. In other words, the energy shift in the XPS spectra was caused by the absence of surface OLA ligands. Choi *et al.* reported a similar energy shift in XPS peaks due to indium–oleate complexes.[33] Generally, OLA and oleic acid are well known as Lewis base molecules due to the presence of an amine or carboxy group. In the case of OLA, the lone pair of the amine group interacts with surface Sn atoms of SnS, theoretically leading to a lower energy shift in the Sn valence states. However, the XPS spectra exhibit an opposite trend and show a higher energy shift with OLA ligands. This suggests that OLA may behave in a Lewis acidic manner, but further investigation is necessary to clarify its role. Fig. 3(d) and (e) show the XPS spectrum of HSNS samples, where a peak shift is observed in the sample annealed at a lower temperature of 400 °C (HSNS-400). Correspondingly, the FT-IR signals (Fig. 3(f)) from OLA disappeared in HSNS-400, which further confirmed the role of OLA in causing a shift to higher binding energy in XPS spectra. On the other hand, the absence of FT-IR signals of OLA in HSNS-400 may also provide evidence for the partial ligand exchange, where OLA is replaced by HMDS. HMDS-derived trimethylsilyl groups ($-Si(CH_3)_3$) function as strong electron-donating ligands, exhibiting superior binding affinity toward surface tin ions compared to OLA molecules under the synthesis conditions. Unfortunately, no signals attributable to HMDS were observed due to insufficient coverage of HMDS molecules on the SnS surfaces.[34,35]

To understand the phase transition process, the relationship between the morphology and crystal phase of individual particles was investigated by TEM, selected area electron diffraction (SAED), and high-resolution TEM (HRTEM). Considering the similarity in morphology evolution and phase transition, OSNS-500 and OSNS-650 were selected for observation here. The TEM image (Fig. 4(a)) of an OSNS-500 particle indicates a tetrahedral shape with slight edge rounding. The corresponding SAED pattern (Fig. 4(b)) revealed the typical pattern of a single crystalline π-SnS with strong diffractions from 002 and 004. The forbidden reflections from 00$l$ ($l$ = 1, 3, 5, … odd numbers) are derived from multiple diffractions due to the relatively large particle thickness (100–300 nm).[36] The 002 systematic diffractions observed in the direction are consistent with the tetrahedrons consisting of (111) surfaces. HRTEM images shown in Fig. 4(c) and (d) exhibit clear and regular lattice fringes. The length of 2.8 nm between 10 periods of the planes is well consistent with the lattice spacing of (400) planes for π-SnS (2.8 Å). Corresponding to the FT-IR results, an amorphous layer can

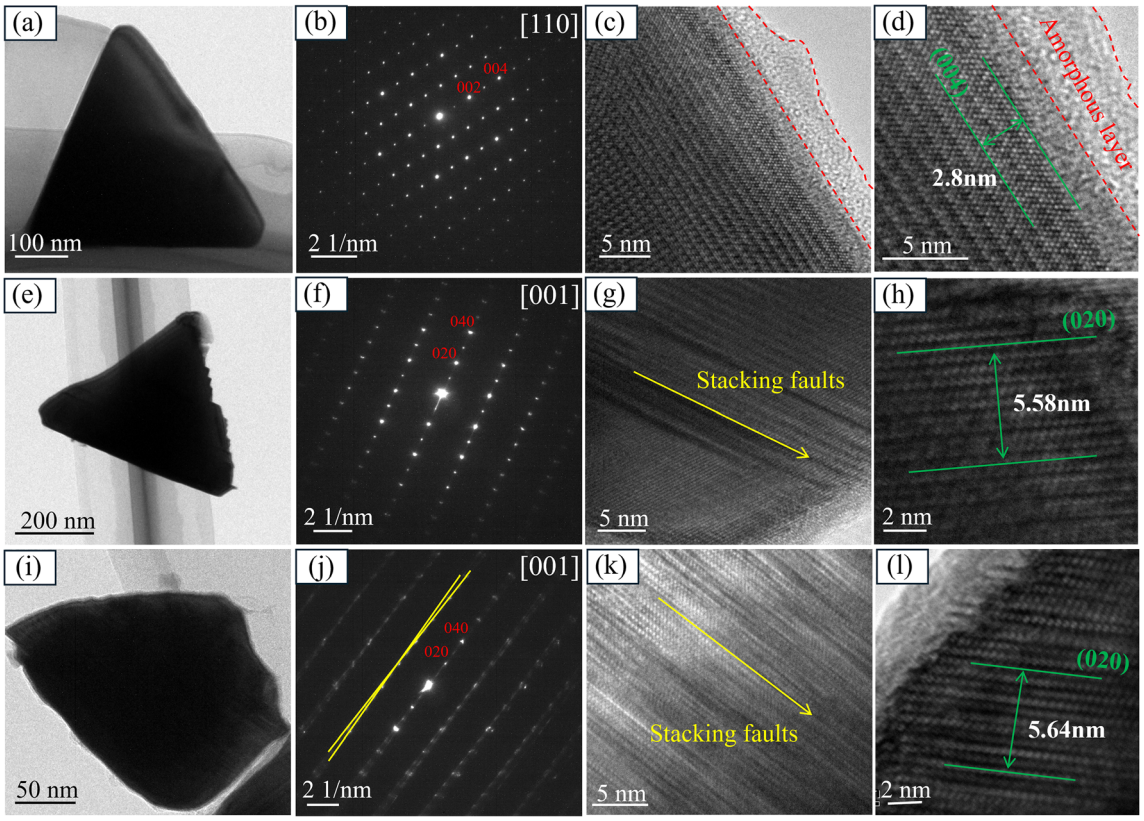


Fig. 4 TEM observations of SnS particles after annealing. (a) Bright field image, (b) SAED pattern with [110] zone axis, and (c and d) HRTEM images of the same particle from OSNS-500. (e and i) Bright-field images. (f and j) SAED pattern with [001] zone axis, and (g and h) (k and l) HRTEM images of OSNS-650.

be observed clearly on the surface. Additional SAED images of OSNS-500 indicating π-SnS are shown in Fig. S5. OSNS-650 particles in Fig. 4(e) and (i) show significant step edges and SAED patterns of α-SnS (Fig. 4(f) and (j)) with [001] zone axis.[37] In addition, the diffraction spots exhibit streaking along [010] direction, indicating the presence of stacking faults, which was further confirmed by the corresponding HRTEM images in Fig. 4(g) and (k).[38] Since the crystal structure of α-SnS consists of layered stacking along [010] direction, it is reasonable to assume that stacking faults form on the (010) planes. Fig. 4(h) and (l) give the distances of 5.58 and 5.64 nm, respectively, for 10 periods of (020) planes, corresponding to the lattice parameter of the *b*-axis in α-SnS (11.2 Å). Notably, Fig. 4(j) shows two sets of diffraction spots, meaning that there are two α-SnS crystal grains along the [001] zone axis and one rotated by a slight angle with the other. This indicates that the single-crystal π-SnS tetrahedrons transformed into polycrystalline α-SnS particles after annealing. The detailed mechanism of such solid-to-solid phase transition behavior will be clarified later. The heterostructure of α-phase and π-phase, as reported by Qin *et al.*,[39] was not observed in our TEM observations.

Based on the above characterizations, the microstructure evolution process through phase transition is discussed. As shown in Fig. 5(a), the as-prepared tetrahedrons of π-SnS single crystal were encapsulated with surface ligands, as confirmed by the FT-IR spectrum. At high temperatures, extensive desorption of surface ligands occurs, resulting in the formation of coordinatively unsaturated surface sites with dangling bonds and localized atomic vacancies. This defective surface configuration triggers spontaneous atomic reorganization, forming a metastable amorphous surface layer. Further thermal activation promotes structural ordering within this amorphous layer, thereby facilitating the heterogeneous nucleation of α-SnS domains at energetically favorable surface sites. These crystalline nuclei subsequently inward propagation of the phase transition front through interface-controlled atomic rearrangement. To maintain the integrity of the tetrahedral shape, the nuclei grow in an epitaxial-like manner along preferred crystallographic orientations, while simultaneously generating a high density of stacking faults to accommodate internal stresses induced by lattice mismatch. Specifically, Fig. 5(b) shows a TEM image and SAED patterns of adjacent grains A, B and C in α-SnS tetrahedrons. The blue region contains the interface between grains B and C. The red arrow indicates the *b*-axis of the original π-SnS tetrahedron. The SAED pattern of A is consistent with the simulated pattern (inset) that grain B rotates 84° clockwise around *b*-axis, indicating that A rotates 84° from B around *b*-axis. Similarly, the grain C rotates 90° from B, confirmed by the SAED pattern from the blue area consisting of both B and C. As shown in Fig. 5(c), we propose a diffusionless-like phase transition similar to the martensitic transformation that does not involve random or diffusive atom movements and

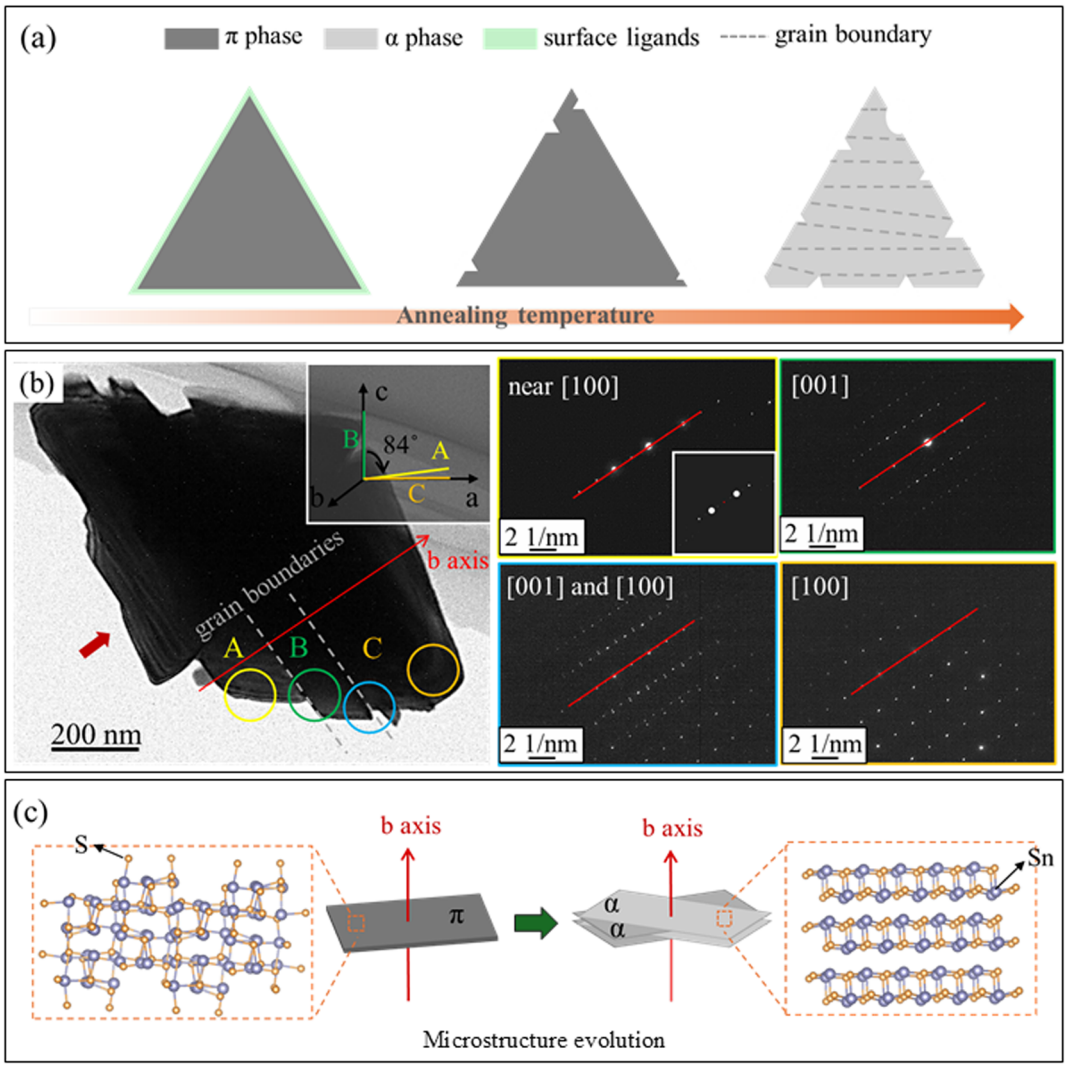


Fig. 5 Schematic illustration of (a) structure evolution of SnS tetrahedrons with increased temperature. (b) TEM image of one SnS tetrahedron (OSNS-650) with various α-phase grains and their SAED patterns. Inset: Simulated SAED pattern corresponding to area A. (c) Microstructure of π phase and α phase.

that results from only small relative displacements of neighboring atoms. Although there is a significant lattice mismatch between the π and α phases, the similarity in atomic bonding prevents the random formation of grains. In other words, the *b*-axis of the transformed α phase retains the direction of the *b*-axis of the original π phase, while the *a*-axis of the α phase undergoes alternating rotations of nearly 90° to form grains. This microstructure might relieve the lattice strain caused by the lattice mismatch between the disordered cubic structure and the ordered layered orthorhombic structure.[5] This transition contributed to large amounts of grain boundaries and stacking faults, similar to those seen in martensitic alloys, resulting in the formation of stacked layered polycrystal α-SnS tetrahedrons. Such diffusionless-like transitions often occur *via* the formation of different microstructural features, many of which have not been observed in SnS previously but represent an important area of investigation for crystallization phenomena.[40–42] Furthermore, the ability to introduce microstructure in SnS allows us to build more complex monochalcogenides that may facilitate better applications.

The SnS particles were employed as photocatalysts for $H_2$ production using the particulate photocatalysis system.[23,43] As shown in Fig. 6(a), hydrogen production increases with longer irradiation time for OSNS. Unfortunately, $H_2$ production in OSNS-400 was only maintained up to 1.5 h. Its efficiency (Fig. 6(b)) significantly reduced to 0.189 μmol $g^{-1}$ $h^{-1}$, approximately 3.9 times lower than 0.740 μmol $g^{-1}$ $h^{-1}$ (OSNS). The reduction is ascribed to the desorption of surface OLA ligands, as confirmed by FT-IR spectra, since no obvious changes in particle morphology and crystal phase were observed. An appropriate amount of surface ligands effectively suppresses carrier recombination and maintains active sites on the particle surface by passivating surface defects and preventing the formation of surface byproducts.[44,45] The capacity of OSNS-500 further decreased to 0.093 μmol $g^{-1}$ $h^{-1}$ and was absent in OSNS-600 and OSNS-650, which is attributed to the formation of the

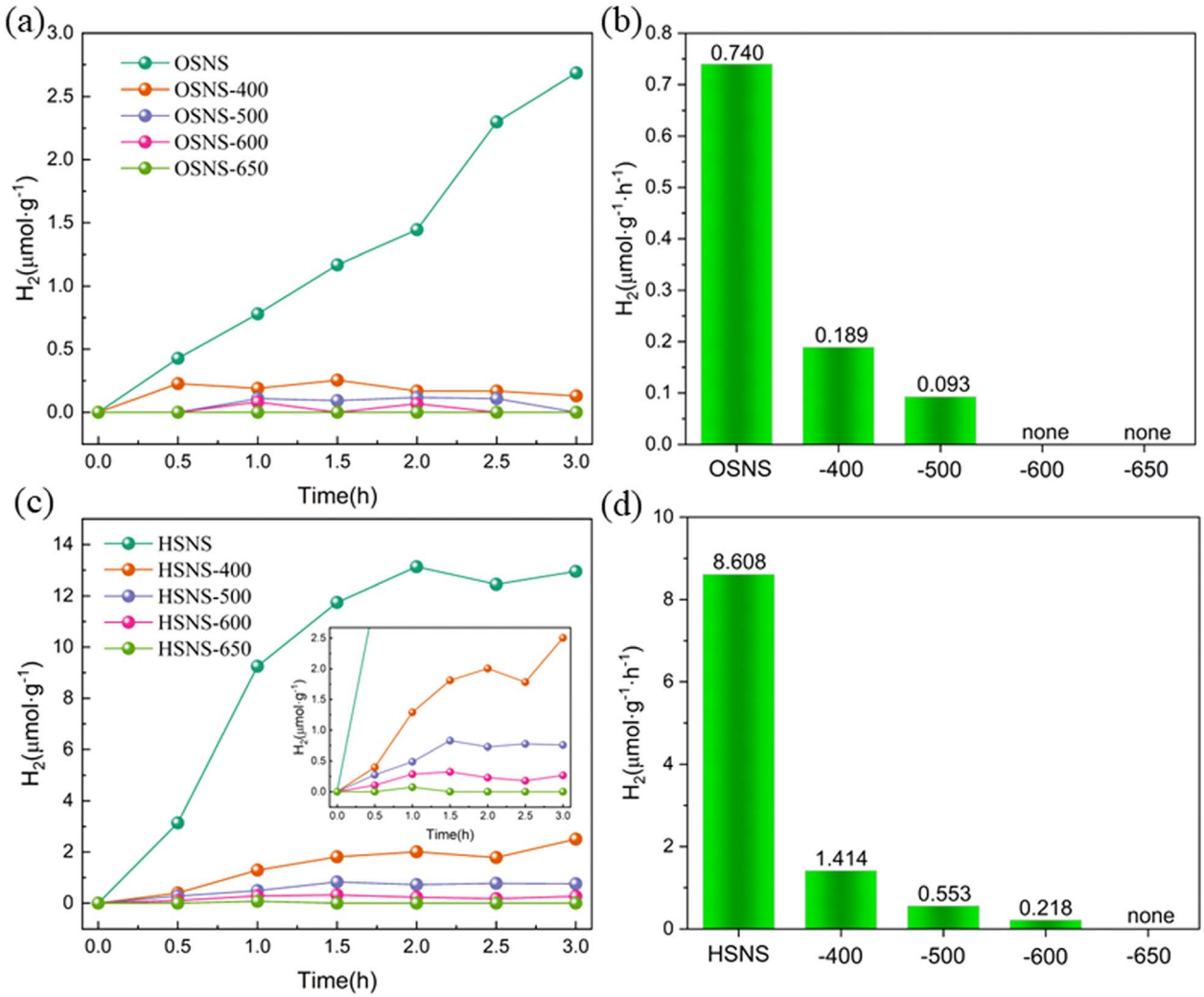


Fig. 6 (a and c) Photocatalytic $H_2$ production with light radiation time and (b and d) $H_2$ generation efficiency for OSNS and HSNS before and after annealing.

polycrystalline α phase. The lattice defects, including stacking faults and grain boundaries, provide numerous centers for carrier recombination, leading to their poor photocatalytic activity. The photocatalytic properties of HSNS before and after annealing are shown in Fig. 6(c) and (d). Consistent with our previous work, HSNS exhibits much better performance of $H_2$ generation, achieving an efficiency of 8.608 μmol $g^{-1}$ $h^{-1}$. After annealing at 400 °C for 10 min (HSNS-400), the efficiency sharply dropped to 1.414 μmol $g^{-1}$ $h^{-1}$. This efficiency is still 7.48 times higher than that of OSNS-400. As speculated in FT-IR spectra, the ligand replacement of OLA by HMDS enables an increased absorption of free carriers, which facilitates the reduction of $H^+$ at the interface. As the temperature increased, the ligands desorbed or decomposed from the surface, and the phase transition occurred, followed by a gradually weakened $H_2$ production capacity.

## 4. Conclusions

In summary, the thermal stability and phase transition behavior of ligand-capped π-SnS particles were studied by comparing the OLA-capped tetrahedrons and HMDS-capped ones upon a post-annealing treatment. Through detailed XRD measurements, it was found the former showed stability up to 400 °C, while the latter showed a higher temperature at 500 °C. At higher temperatures, the transition from π phase to α phase occurred and was completed at 650 °C within 10 min. In particular, a "reversible" phase transition with annealing time was observed for the first time. Through the analysis of TEM and SAED patterns, we proposed a martensite-like phase transformation from π phase to α phase in ligand-capped SnS tetrahedrons. The phase transition is triggered by the desorption of surface ligands, which initiates the rearrangement of surface atoms and thus forms multiple nucleation sites for the ground state α phase on the surface under thermal activation. The subsequent transition excites the chain rearrangement of adjacent atoms to form α-SnS grains with large amounts of boundaries and stacking faults to balance the severe lattice mismatches. However, the boundaries and stacking faults supply numerous sites for carrier recombination, leading to the poor photocatalytic $H_2$ evolution performance of the polycrystal

α-SnS. This work reports a martensite-like phase transformation phenomenon in SnS particles for the first time and provides a new strategy for controlling the stability of metastable particles by regulating surface ligands, which will significantly stimulate the interest of ligand-capped particles and their construction of microstructure in various applications.

## Author contributions

X. Du: conceptualization, formal analysis, investigation, methodology, visualization, writing – original draft, writing – review & editing. K. Kazumi: formal analysis and performance of TEM. T. Utsunomiya: formal analysis and performance of FT-IR. I. Sumiyoshi: formal analysis. Y. Nose: conceptualization, formal analysis, methodology, funding acquisition, resources, supervision, writing – review & editing.

## Conflicts of interest

There are no conflicts of interest to declare.

## Data availability

The data supporting this article have been included as part of the SI.

Supplementary information is available. Additional SAED characterizations for single particle and UV-Vis transmittance spectra are also included. See DOI: **https://doi.org/10.1039/d5ra03669k**.

## Acknowledgements

This work was partially supported by JSPS KAKENHI (No. 21K19033 and 23K26432). The authors thank Mr Nobuharu Sasaki for his help with the TEM observation. The author X. D. thanks the financial support from the China Scholarship Council.

## References

1 R. E. Abutbul, E. Segev, L. Zeiri, V. Ezersky, G. Makov and Y. Golan, *RSC Adv.*, 2016, **6**, 5848–5855.
2 R. E. Abutbul, E. Segev, U. Argaman, G. Makov and Y. Golan, *Adv. Mater.*, 2018, **30**, 1706285.
3 A. Rabkin, S. Samuha, R. E. Abutbul, V. Ezersky, L. Meshi and Y. Golan, *Nano Lett.*, 2015, **15**, 2174–2179.
4 P. K. Nair, A. R. Garcia-Angelmo and M. T. S. Nair, *Phys. Status Solidi A*, 2016, **213**, 170–177.
5 J. M. Skelton, L. A. Burton, F. Oba and A. Walsh, *APL Mater.*, 2017, **5**, 036101.
6 A. R. Garcia-Angelmo, R. Romano-Trujillo, J. Campos-Álvarez, O. Gomez-Daza, M. T. S. Nair and P. K. Nair, *Phys. Status Solidi A*, 2015, **212**, 2332–2340.
7 S. S. Hegde, V. Talapatadur, S. Vinoth, V. P. Priyanka, P. Murahari and K. Ramesh, *Mater. Today: Proc.*, 2022, **62**, 5583–5588.
8 A. J. Biacchi, D. D. Vaughn and R. E. Schaak, *J. Am. Chem. Soc.*, 2013, **135**, 11634–11644.
9 L. A. Burton and A. Walsh, *J. Phys. Chem. C*, 2012, **116**, 24262–24267.
10 M. S. Mahdi, H. S. Al-Arab, A. Hmood and M. Bououdina, *Opt. Mater.*, 2022, **123**, 111910.
11 F. D. B. Sánchez, M. T. S. Nair and P. K. Nair, *Semicond. Sci. Technol.*, 2023, **39**, 015003.
12 A. A. Voznyi, O. V. Bilousov, B. Landeke-Wilsmark, J. Keller, J. Ren, S. L. Zhang and C. Hägglund, *ACS Appl. Energy Mater.*, 2021, **4**, 8085–8097.
13 K. Jeganath, N. J. Choudhari, G. S. Pai, A. Rao and Y. Raviprakash, *Mater. Sci. Semicond. Process.*, 2020, **113**, 105050.
14 U. Chalapathi, B. Poornaprakash and S. H. Park, *Superlattices Microstruct.*, 2017, **103**, 221–229.
15 S. Polivtseva, A. Katerski, E. Kärber, I. Oja Acik, A. Mere, V. Mikli and M. Krunks, *Thin Solid Films*, 2017, **633**, 179–184.
16 R. E. Abutbul, A. R. Garcia-Angelmo, Z. Burshtein, M. T. S. Nair, P. K. Nair and Y. Golan, *CrystEngComm*, 2016, **18**, 5188–5194.
17 B. K. Patra, A. K. Guria, A. Dutta, A. Shit and N. Pradhan, *Chem. Mater.*, 2014, **26**, 7194–7200.
18 S. S. Hegde, B. S. Surendra, V. Talapatadur, P. Murahari and K. Ramesh, *Chem. Phys. Lett.*, 2020, **754**, 137665.
19 S. S. Hegde, P. Murahari, B. J. Fernandes, R. Venkatesh and K. Ramesh, *J. Alloys Compd.*, 2020, **820**, 153116.
20 E. C. Greyson, J. E. Barton and T. W. Odom, *Small*, 2006, **2**, 368–371.
21 E. Segev, R. E. Abutbul, U. Argaman, Y. Golan and G. Makov, *CrystEngComm*, 2018, **20**, 4237–4248.
22 H. Fridman, N. Barsheshet, S. Kolusheva, T. Mokari, S. Hayun and Y. Golan, *Nanoscale*, 2023, **15**, 8881–8887.
23 X. Du, I. Sumiyoshi, Y. Nose and S. Ikeda, *Int. J. Hydrogen Energy*, 2024, **95**, 309–316.
24 Z. Deng, D. Han and Y. Liu, *Nanoscale*, 2011, **3**, 4346–4351.
25 B. Ghosh, R. Bhattacharjee, P. Banerjee and S. Das, *Appl. Surf. Sci.*, 2011, **257**, 3670–3676.
26 P. Sinsermsuksakul, L. Sun, S. W. Lee, H. H. Park, S. B. Kim, C. Yang and R. G. Gordon, *Adv. Energy Mater.*, 2014, **4**, 1400496.
27 N. Aparna, R. S. Philip and M. Mathew, *Mater. Today Sustain.*, 2024, **27**, 100941.
28 S. K. Gautam, J. Singh, D. K. Shukla, E. Pippel, P. Poddar and F. Singh, *Acta Mater.*, 2018, **146**, 253–264.
29 W. Tian, J. Han, N. Li, D. Chen, Q. Xu, H. Li and J. Lu, *Chin. J. Catal.*, 2024, **64**, 166–179.
30 M. Dogrusoz and R. Demir-Cakan, *Int. J. Energy Res.*, 2020, **44**, 10809–10820.
31 G. K. Veerasubramani, M. S. Park, J. Y. Choi and D. W. Kim, *ACS Appl. Mater. Interfaces*, 2020, **12**, 7114–7124.
32 A. Stavrinadis, J. M. Smith, C. A. Cattley, A. G. Cook, P. S. Grant and A. A. R. Watt, *Nanotechnology*, 2010, **21**, 185202.
33 M. J. Choi, L. K. Sagar, B. Sun, M. Biondi, S. Lee, A. M. Najjariyan, L. Levina, F. P. G. Arquer and E. H. Sargent, *Nano Lett.*, 2021, **21**, 6057–6063.

34 S. Mourdikoudis and L. M. Liz-Marzán, *Chem. Mater.*, 2013, **25**, 1465–1476.
35 B. S. Yadav, N. Hsan, A. K. Vishwakarma, A. K. Singh, S. Kumar, J. Koh, P. K. Dutta and N. Kumar, *Solid State Sci.*, 2024, **150**, 107500.
36 O. Molnárová, O. Tyc, M. Klinger and P. Šittner, *Mater. Charact.*, 2024, **214**, 114084.
37 U. P. Gawai, D. K. Gaikwad, S. L. Patil, K. K. Pandey, N. P. Lalla and B. N. Dole, *RSC Adv.*, 2020, **10**, 21277–21282.
38 Y. Chen, T. Burgess, X. An, Y. W. Mai, H. H. Tan, J. Zou, S. P. Ringer, C. Jagadish and X. Liao, *Nano Lett.*, 2016, **16**, 1911–1916.
39 Y. Qin, Y. Liang, C. Zhou and Y. Bai, *Sens. Actuators, B*, 2024, **404**, 135285.
40 D. W. Yee, M. S. Lee, J. An and R. J. Macfarlane, *J. Am. Chem. Soc.*, 2023, **145**, 6051–6056.
41 S. Schwabe, R. Niemann, A. Backen, D. Wolf, C. Damm, T. Walter, H. Seiner, O. Heczko, K. Nielsch and S. Fähler, *Adv. Funct. Mater.*, 2021, **31**, 2005715.
42 R. C. Pond and S. Celotto, *Int. Mater. Rev.*, 2003, **48**, 225–245.
43 B. J. Ng, L. K. Putri, X. Y. Kong, Y. W. Teh, P. Pasbakhsh and S. P. Chai, *Adv. Sci.*, 2020, **7**, 1903171.
44 M. A. Uddin, J. K. Mobley, A. A. Masud, T. Liu, R. L. Calabro, D.-Y. Kim, C. I. Richards and K. R. Graham, *J. Phys. Chem. C*, 2019, **123**, 18103–18112.
45 S. H. Noh, K. H. Lee, H. S. Yang, J. Jung, E. H. Suh, J. G. Oh, U. Paik, S. C. Park and J. Jang, *Chem. Eng. J.*, 2024, **481**, 148127.